Purdue University
Purdue e-Pubs

CTRC Research Publications | Cooling Technologies Research Center

2021

Asymmetric Solidification During Droplet Freezing in the Presence of a Neighboring Droplet

J. E. Castillo
Purdue University

Y. Huang
Shanghai Jiao Tong University

Z. Pan
Shanghai Jiao Tong University

J. A. Weibel
Purdue University, jaweibel@purdue.edu

Follow this and additional works at: https://docs.lib.purdue.edu/coolingpubs

Castillo, J. E.; Huang, Y.; Pan, Z.; and Weibel, J. A., "Asymmetric Solidification During Droplet Freezing in the Presence of a Neighboring Droplet" (2021). *CTRC Research Publications.* Paper 373.
http://dx.doi.org/https://doi.org/10.1016/j.ijheatmasstransfer.2021.121134

This document has been made available through Purdue e-Pubs, a service of the Purdue University Libraries. Please contact epubs@purdue.edu for additional information.

Asymmetric Solidification during Droplet Freezing in the Presence of a Neighboring Droplet

Julian E. Castillo[1], Yanbo Huang[2], Zhenhai Pan[2], and Justin A. Weibel[1,*]

[1]School of Mechanical Engineering, Purdue University, West Lafayette IN 47907 USA.

[2]School of Mechanical Engineering, Shanghai Jiao Tong University, Shanghai, China.

[*] Corresponding author.

E-mail addresses: castil19@purdue.edu (Julian E. Castillo), hyb728@sjtu.edu.cn (Yanbo Huang) panzhh@sjtu.edu.cn (Zhenhai Pan), and jaweibel@purdue.edu (Justin A. Weibel)

Abstract

A supercooled liquid droplet that freezes on a cold substrate interacts with the local surroundings through heat and mass exchange. Heat loss occurs to the substrate via conduction and at the droplet interface via evaporative cooling, diffusion, and convection. In a group of many droplets, these interactions are believed to be responsible for inter-droplet frost propagation and the evaporation of supercooled neighboring droplets. Furthermore, interactions between a standalone freezing droplet and its surroundings can lead to the formation of condensation halos and asymmetric solidification induced by external flows. This paper investigates droplet-to-droplet interactions via heat and mass exchange between a freezing droplet and a neighboring droplet, for which asymmetries are observed in the final shape of the frozen droplet. Side-view infrared (IR) thermography measurements of the surface temperature for a pair of freezing droplets, along with three-dimensional numerical simulations of the solidification process, are used to quantify the intensity and nature of these interactions. Two droplet-to-droplet interaction mechanisms causing asymmetric freezing are identified: (1) non-uniform evaporative cooling on the surface of the freezing droplet caused by vapor starvation in the air between the droplets; and (2) a non-uniform thermal resistance at the contact area of the freezing droplet caused by the heat conduction within the neighboring droplet. The combined experimental and numerical results show that the size of the freezing droplet relative to its neighbor can significantly impact the intensity of the interaction between the droplets and, therefore, the degree of asymmetry. A small droplet freezing in the presence of a large droplet, which blocks vapor from freely diffusing to the surface of the small droplet, causes substantial asymmetry in the solidification process. The

droplet-to-droplet interactions investigated in this paper provide insights into the role of latent heat dissipation during condensation frosting.

Keywords: droplet freezing; infrared thermography; water vapor distribution; recalescence; solidification

Nomenclature

A	area (m^2)
C	vapor molar concentration (mol / m^3)
c_p	heat capacity (J / kg K)
D	diffusion coefficient in air (m^2 / s)
E_{mushy}	mushy zone constant (kg m^3 / s)
h_s	sensible enthalpy (J / kg)
h_{fg}	latent heat of evaporation (J / kg)
h_{fs}	latent heat of solidification (J / kg)
H	total latent heat (J / kg)
k	thermal conductivity (W / m K)
M	molecular weight (kg / mol)
m''	mass flux (kg / m^2 s)
$\vec{n}$	unit vector pointing normal to the droplet interface
p	pressure (N / m^2)
R	universal gas constant (J / mol K)
s	length along the arc of the droplet-gas interface (m)
S_m	mass source term (kg / m^3 s)
S_h	energy source term (W / m^3)
S_p	momentum sink term (kg/m^2 s)
t	time (s)
T	temperature (°C)
v	droplet volume (m^3)

$\vec{V}$	fluid flow velocity (m / s)
q	heat transfer rate (W)
q''	heat flux (W/m^2)
x	ice fraction

Greek

α	thermal diffusivity (m^2 / s)
β	liquid fraction
δ	thickness of hydrodynamic boundary layer (m)
ε	constant in the momentum sink term
Γ	diffusivity coefficient (kg/ m s)
μ	dynamic viscosity (N s/ m^2)
ρ	density (kg / m^3)
ω	fraction of water-air mixture
ξ	any thermophysical property

Subscripts

1	phase 1
2	phase 2
∞	far-field
air	air
atm	at atmospheric conditions
c	the contact area between droplet and substrate
cell	computational cell at the droplet-gas interface
eq	at the equilibrium freezing temperature (0 °C for water)
exp	experiment
g	gas (vapor/air mixture)
l	liquid
liq	at liquidus condition
lv	liquid-gas interface
n	component in direction normal to the liquid-gas interface

v	vapor
p	porous-like media
s	solid substrate
sat	saturated
sol	at solidus condition
ref	reference
rec	recalescence
water	water

1.0. Introduction

Ice accretion on the surfaces of aircraft [1], wind turbine blades [2], heat exchangers [3,4], power transmission lines [5], and other infrastructure [6–8] can compromise the safety, efficiency, and cost of operation. De-icing technologies that rely on active heating or mechanical means to remove ice from the surfaces, although widely used, are costly and inefficient [9]. Alternatively, passive de-icing technologies, such as spreading anti-icing materials (e.g., salts and glycols) are cheaper than active methods but pose an environmental threat to ecosystems that rely on the ground and waters where anti-freezing substances are drained [10–12]. Engineering the surface morphology and chemical affinity with water have the potential to passively prevent the formation of ice and subsequent frost propagation [13–15]. Superhydrophobic surfaces can delay the onset of heterogeneous nucleation of ice [16] and also the propagation of frost by promoting shedding of condensate before freezing occurs [17]. However, once ice nucleation has occurred inside any droplet on hydrophobic and superhydrophobic surfaces, ice inevitably percolates throughout the surface [18]. To delay frost propagation via spatial control of the water vapor concentration near the substrate, such as by using chemically patterned hydrophilic/hydrophobic and anti-freezing substances [19,20], requires prediction of the coupled heat and mass transfer processes occurring between neighboring liquid and ice surfaces that are not well understood [21,22].

When a droplet undergoes freezing on a cooled substrate, heat and mass transfer between the droplet and its surroundings may significantly influence the freezing process. At the onset of droplet freezing, evaporative cooling at the interface of the droplet can induce homogeneous ice embryo nucleation as opposed to the commonly observed heterogeneous nucleation near the

substrate [23]. After nucleation, ice crystals rapidly propagate throughout the droplet; during this recalescence process, the droplet increases in temperature to the equilibrium freezing point in the order of tens of milliseconds. It is often assumed that all latent heat released due to the formation of ice crystals during recalescence is transformed into the sensible energy required to increase the temperature of the droplet to the equilibrium freezing point [22,24,25]. However, a portion of the latent heat released can be lost through evaporation and heat conduction to the substrate, as exemplified by some specific observations. For example, latent heat release during droplets freezing on substrates with low thermal conductivity can cause sufficient evaporation such that microdroplets condense in the form of a halo around the contact line of the freezing droplet [26]. Also, liquid films undergoing recalescence on substrates with higher thermal conductivities will exhibit higher rates of crystal growth [27], indicating the influence of substrate conduction on the process. We have recently demonstrated that considering heat losses to the substrate and ambient air during recalescence is critical, and only by including these losses can simulations closely match measurements of the droplet temperatures during solidification[28].

Following droplet recalescence, the fraction of liquid remaining in the droplet solidifies through a much slower process that is controlled by the latent heat released to the substrate via conduction and through the droplet interface via convection. In our recent work [28], we quantitatively determined the amount of the latent heat released, during solidification of a single droplet, that is transferred to the substrate versus that lost through the droplet-air interface due to evaporative cooling, heat diffusion, and natural convection. In the absence of convective shear flow, droplet solidification occurs uniformly and at a rate that depends on the droplet volume, contact angle, and substrate cooling rate [24,25,28,29]. Under this condition, droplets solidify to form a tapered conical tip that is symmetric with respect to the droplet centerline prior to recalescence [30,31]. In contrast, when droplet freezing occurs in presence of shear flow, non-uniform evaporative cooling on the interface causes asymmetric propagation of the solidification front. A cold air flow from left to right causes the left side of the droplet to solidify at a faster rate, resulting in a final droplet shape with an asymmetric tip pointed to the right [23,32,33]. Under exceptionally low vapor pressure (~3% RH) and high cooling rates at the droplet-gas interface, non-uniform solidification from the droplet-gas interface and droplet contact area with the substrate can lead to spontaneous dislodging [34]

In a population of supercooled liquid droplets resting on a substrate, it is believed that

interactions between freezing droplets and their surroundings lead to the evaporation of neighboring droplets. Water evaporated from supercooled liquid droplets condenses on neighboring frozen droplets and promote the growth of ice bridges directed towards the liquid droplets that are being evaporated. Frost propagates in the directions where ice bridges can connect freezing droplets to supercooled liquid neighbors before they complete evaporate. Two possible governing mechanisms for the evaporation of neighboring droplets have been proposed. First is the water vapor pressure gradient induced by the saturation pressure difference in the air between a frozen droplet and liquid droplet. It has also been proposed that local heating of the substrate, caused by latent heat release from the freezing droplet, can cause this evaporation. As illustrated in the qualitative schematic diagram presented in Figure 1, a fraction of the latent heat released will be lost to the substrate, while some portion of the heat will be lost to the ambient air through the droplet interface. The relative strength of the two possible mechanisms depends on the relative sizes and separation between the droplets [35]. Since the latent heat of solidification of water at 0 °C is much smaller than the latent heat of vaporization ($h_{sf} \ll h_{fg}$), equally-sized droplets cannot release enough latent heat to completely evaporate their neighbors. Whereas large-scale droplets ($R \sim$ 1 mm) can release enough heat to evaporate smaller droplets ($R \sim$ 1 μm). For example, it has been observed that the latent heat released during solidification of a millimeter-size droplet on a substrate with high thermal conductivity can induce rapid evaporation of surrounding micrometer-size droplets [26]. Whereas the latent heat released to the substrate by a droplet with a radius of $R \sim$ 1 mm is not large enough to induce the evaporation of similarly sized neighboring droplets [22]. To the date, the two mechanisms for droplet-to-droplet interactions during droplet freezing have been considered separately. Furthermore, the fraction of heat that is transferred to a neighboring droplet, critical to understanding of frost propagation, has not been quantitatively assessed. A better understanding of the nature of the interactions between freezing droplets could also provide further insights on the transport mechanism that govern the propagation of frost in a population of droplets exposed to a low-pressure environment, where the local vapor concentration has been proposed to be an important mechanism affecting frost propagation [36].

This paper investigates the relative significance of the heat and mass transport mechanism that govern the interactions between pairs droplets freezing on a cooled substrate. The transient temperature map over the surface of a freezing droplet is measured simultaneously with that of a neighboring droplet using infrared (IR) thermography. These data are employed to quantify the

fraction latent heat transferred from a freezing droplet to its neighbor. Experiments are performed for cases where the two droplets are similar in size and where one of the droplets is much larger than its neighbor. These results are used to demonstrate the impact of the relative droplet size on the intensity of the interactions. A 3D model for numerical simulation of droplet solidification, as well as heat and mass transfer between these pairs of freezing droplets, is used to quantify the relative strength of the interactions due to mass transport through the ambient air versus heat transport through the substrate. The results demonstrate that droplet-to-droplet interactions during freezing are responsible for asymmetrical solidification.

2.0. Experimental description

Temperature measurements on the surfaces of a pair of adjacent freezing droplets were acquired using IR thermography in a custom-made experimental facility previously detailed in Ref [28] for characterization of single-droplet freezing. This section provides a brief description of the test facility and the changes in procedure to enable simultaneous infrared temperature measurements on the surface of pairs of droplets. A schematic diagram of the test facility, which is capable of cooling a substrate below freezing while maintaining uniform background radiation, is provided in Figure 2. The experimental facility consists of a black painted (ColorMasterTM Flat Black, Krylon; emissivity of 0.97) aluminum enclosure cooled to sub-ambient temperature using two temperature-controlled thermoelectric stages (CP-031, TE Technology, Inc.). The substrate, which is positioned inside the metallic enclosure, is attached to a sample holder positioned on top of a third cooling device (ZT8, Laird Technologies) which allows cooling the substrate to sub-freezing temperatures. The thermoelectric plate maintains the substrate at a setpoint temperature measured using a 2-wire Pt1000 RTD (PRTF-10-2-100-1/4-12-E-GG, Omega) inserted in the sample holder. The test section is mounted on micrometer stages to allow easy focusing during the infrared measurements.

Smooth hydrophobic silicon substrates prepared as described in Ref [28] were attached to the sample holder using carbon conductive double-sided tape (PELCO Image Tabs). Subsequently, two adjacent droplets were deposited using a pipette. The thermoelectric stages are set to maintain the enclosure at -1.5 °C. After ~15 min, once the entire test section has cooled down, the sample thermoelectric controller is turned on and set to -9.0 °C. After ~4 min, the temperature measured

by the RTD reaches a constant value within ± 2% of the setpoint. After ~10 min, ice nucleation occurs within the droplets sequentially.

An IR camera (SC7650, FLIR) is used to record the transient temperature of the surfaces of the droplets at a frame rate of 100 fps. Frames are captured at a spatial resolution of 0.038 ± 0.004 mm/pixel (uncertainty taken as the standard deviation over 8 measurements) using a 50 mm lens (Nyctea, Janos) connected to the camera body with a 38 mm extension tube. The IR camera was calibrated pixel-by-pixel over a range of temperatures from -10 °C to 4.0 °C using a custom-made black body radiator, where the signal intensity of each pixel is fitted as function of the set-point temperature with a fourth-order polynomial equation. Errors in the surface temperature of the droplets caused by background radiation and non-uniform emissivity of the surface were corrected using the difference between the temperature of the droplet after recalescence and the equilibrium temperature for freezing (0 °C). Further details on the calibration procedure are described in Ref [28].

Simultaneous surface temperature recordings on the surfaces of two droplets are reported in this paper for two cases. A schematic representation of the two cases considered is provided in Figure 3. The first case (S) considers a pair of droplets similar in size, with volumes of 2.88 μL (droplet S1) and 2.52 μL (droplet S2), and a center-to-center distance of 2.38 mm. Droplet S1 solidifies while droplet S2 remains supercooled liquid, followed by the solidification of droplet S2. The second case (D) considers a larger 8.98 μL droplet (D1) with a smaller 0.76 μL neighboring droplet (D2) located 2.40 mm away that solidify in the same sequence.

3.0. Numerical Model Description

Numerical simulations of the sequential solidification of a droplet and its neighbor are performed using ANSYS Fluent [37] with the boundary conditions and droplet volumes the same as the two freezing experiments described in Section 2.0. Figure 3 illustrates the two cases that are simulated. Matching the experiments, case S considers the solidification of droplet S1 while droplet S2 remains in liquid state (left panel) followed by the solidification of droplet S2 (right panel). Case D similarly simulates the sequential solidification of droplets D1 and D2. For each case, a three-dimensional model with fixed grid is used to simulate: solidification at the freezing front; heat transfer and fluid flow within the domain of the solidifying droplet; coupled heat and mass transfer at the interface of the solidifying droplet with the gas domain; heat conduction within

the solid substrate; and heat and mass transfer in the surrounding gas domain. For the neighboring (solid or liquid) droplet, heat conduction within the droplets as well as coupled heat and mass transfer at the interface with the gas domain are also considered. The computational domain shown with a mesh overlay and key phases, interfaces, and boundaries indicated, is illustrated in Figure 4. All the material properties used in the simulation are summarized in Table 1. A few assumptions in the implementation of the model were used to reduce the level of complexity of the simulations. The numerical simulations neglect the volume change due to water expansion during freezing, which is known to have negligible influence on the thermal resistance to heat flow in the frozen droplet [28]. Changes in the volume of the neighboring droplet due to evaporation/condensation are also neglected as they are negligible compared to the total droplet volumes. Therefore, all the cases use a fixed-grid computational domain, where the shape of the droplets remain unchanged with time. The model description provided in the following sections is modified from Ref [28] to accommodate for a third spatial dimension and to include the neighboring droplet.

3.1. Droplet domain during solidification

The enthalpy-porosity formulation [38,39] implemented in the ANSYS Fluent [37] Solidification/Melting model is used to simulate phase change within the domain of the solidifying droplet. In this formulation for solidification, the liquid of fraction (β) within each cell in the computational domain follows a linear relationship with the temperature (T):

$$\beta = \begin{cases} 0 & T < T_{sol} \\ \dfrac{T - T_{sol}}{T_{liq} - T_{sol}} & T_{sol} < T < T_{liq} \\ 1 & T > T_{liq} \end{cases} \tag{1}$$

where T_{sol} and T_{liq} are the liquidus and solidus temperatures for water, and β varies between 0 $\leq \beta \leq$ 1 depending on the fraction of liquid within the cell, with β = 1 indicating that all the water within the cell is in liquid state and β = 0 indicating that the cell is entirely frozen. Any thermophysical property ξ, such as specific heat or thermal conductivity, is expressed in the terms of the liquid fraction as:

$$\xi = \begin{cases} \xi_s & T < T_{sol} \\ (1-\beta)\xi_s + \beta\xi_l & T_{sol} < T < T_{liq} \\ \xi_l & T > T_{lid} \end{cases} \quad (2)$$

where ξ_l and ξ_s are the values of the property in the liquid and solid states, respectively. The mass and momentum equations are simplified by assuming that the fluid flow is laminar in the regions where β = 1 and the fluid flow is assumed to be a porous-like fluid flow within the regions of the droplet that are solidified partially (0 < β < 1). Under these assumptions, the continuity and momentum equations are expressed as:

$$\rho_l \nabla \vec{V}_l = S_{m,l} \quad (3)$$

$$\rho_l \vec{V}_l \cdot \nabla \vec{V}_l = -\nabla p_l + \mu_l \nabla^2 \vec{V}_l + S_p \quad (4)$$

where $\vec{V}$ is fluid velocity, μ_l is the viscosity of water (μ_l = 1.003 x 10 $^{-3}$ kg/m s), $S_{m,l}$ is a mass source term related to the transport across the interface, which is discussed in Section 3.3, and S_p is a momentum sink term that pertains to forces created by the displacement of the solidification front. By further assuming that the flow within the mushy region is governed by Darcy's law, S_p is defined as:

$$S_p = \frac{(1-\beta)^2}{\beta^3 + \varepsilon} E_{mushy} \vec{V}_l \quad (5)$$

where ε is set equal to 0.001 to prevent division by zero when $\beta \to 0$ and E_{mushy} is a constant that depends on the morphology of the porous media; in this simulation E_{mushy} is set equal to 1×10^5 to control the rate at which the velocity in front of the mushy zone transitions to zero as the solidification front advances.

Using the definition of sensible enthalpy h, the energy transport within the droplet domain is modeled using the energy equation expressed as:

$$\frac{\partial}{\partial t}(\rho h) + \nabla \cdot (\rho \vec{V} h) = \nabla \cdot (\alpha \nabla h) + S_h + S_{h,l} \quad (6)$$

where the energy source term S_h in this equation is derived from the enthalpy formulation of convection-diffusion phase change and is expressed as [40]:

$$S_h = \frac{\partial(\rho \Delta H)}{\partial t} + div\left(\rho \vec{V} \Delta H\right) \tag{7}$$

where the total enthalpy H associated with each cell is calculated as the sum of the sensible enthalpy h and latent heat of the fraction of liquid remaining in the cell ($\Delta H = \beta h_{fs}$), with h_{fs} being the latent heat of solidification (h_{fs} = 335000 J/kg for water), and the source term $S_{h,l}$ is related to the energy transfer across the interface as described in Section 3.3.

3.2. Neighboring droplet, substrate, and surrounding gas domains

Transient heat transport within the neighboring droplet is modeled assuming that thermophysical properties do not vary within the range of temperatures considered. Under this assumption the energy equation can be expressed as:

$$\frac{\partial T}{\partial t} = \alpha \nabla^2 T \tag{8}$$

where α is the thermal diffusivity of water or ice depending on the case considered (i.e., supercooled liquid or frozen solid neighbor). Equation (8) is also used to simulate heat transfer within the solid substrate domain, with the thermal diffusivity of silicon given in Table 1.

The continuity, momentum, and energy equations for fluid flow in the gas domain are respectively:

$$\nabla\left(\rho_g \vec{V}_g\right) = S_{m,l} \tag{9}$$

$$\rho_g \vec{V}_g \cdot \nabla \vec{V}_g = -\nabla p_g + \mu_g \nabla^2 \vec{V}_g + \rho_g \vec{g} \tag{10}$$

$$\rho c_p \vec{V} \cdot \nabla T = k \nabla^2 T + S_{h,g} \tag{11}$$

where $S_{m,g}$ and $S_{h,g}$ are mass and energy terms later described in Section 3.3, and μ_g is the viscosity of air (μ_g = 1.789 x 10^{-5} kg/m s). Additionally, it is assumed that the air-vapor mixture in the gas domain follows the ideal gas law; with these simplifications the density of the vapor-air mixture ρ_g can be is expressed as:

$$\rho = C_v M_v + \left(\frac{p_{atm}}{RT} - C_v\right) M_{air} \tag{12}$$

where M_{water} is the molecular weight of water (M_{water} = 0.018 kg/mol), M_{air} is the molecular weight of dry air (M_{air} = 0.029 kg/mol), and C_v is the mole concentration of water vapor in the mixture. To solve for the vapor transport via diffusion and convection in the gas domain, the following governing equation is implemented:

$$\vec{V} \cdot \nabla C_v - \nabla \cdot \left(D \cdot \nabla C_v \right) = 0 \tag{13}$$

where the temperature-dependent diffusion coefficient D in equation (13) is given by:

$$D\left(T\right) = D_{ref} \left(\frac{T}{T_{ref}} \right)^{1.5} \tag{14}$$

Additional details on the implementation of equation (13) using user-defined scalar (UDS) functions in ANSYS Fluent are described in Ref [28].

3.3. Droplet-gas interfaces

Heat and mass transfer through the droplet-gas interfaces of both the solidifying droplet and its neighbor are modeled. The effects of capillary pressure for the millimeter scale droplets can be neglected [41]. The interfacial resistances to condensation and evaporation along the surfaces of the droplets are also neglected because, in presence of non-condensable gases, the resistance to water vapor diffusion dominates over interfacial resistance. Thus, the local saturation pressure of vapor is calculated using the temperature of the droplet-gas interface. At a given interface temperature, the saturation pressure will also depend on the local fraction of ice, as the saturation pressure above of an ice surface is smaller than that above a supercooled liquid surface [42]. To account for the effect of the local fraction of ice on the local saturation pressure, cells on the surface of the droplet-air interface of the solidifying droplet above 0 °C are treated as liquid, whereas cells below 0 °C are treated as solid ice. Expressions for the saturated vapor pressure above ice and supercooled liquid surfaces, as well as further details on the calculation of the content of water inside the air domain, are provided in Ref [28].

Shear stress along both sides of the liquid-gas interface is set as zero, and the vapor flux across the interface, which can be caused by condensation or evaporation, is expressed as:

$$m'' = M_v \left(-D\vec{n} \cdot \nabla C_v + v_n C_v \right) \tag{15}$$

where the first term on the right-hand side of the equation is the vapor transport due to mass diffusion, and the second term represents mass convection by Stefan flow. The transport of air across droplet-air interface is set to zero:

$$0 = M_g \left(-D\vec{n} \cdot \nabla \left(C_g - C_v \right) + v_n \left(C_g - C_v \right) \right) \tag{16}$$

The velocity of the vapor crossing the interface can therefore be written as:

$$v_n \big|_{lv} = -\frac{1}{C_g - C_v} D\left(\vec{n} \cdot \nabla C_v \right) \tag{17}$$

Equations (15) and (17) are coupled to find an expression for the mass flux at the interface:

$$m'' = -\frac{MD}{1 - C_v / C_g} \left(\vec{n} \cdot \nabla C_v \right) \big|_{lv} \tag{18}$$

where the vapor molar concentration in the gas and the vapor at the interface are respectively calculated as $C_g \big|_{lv} = p_{atm} / RT_{lv}$ and $C_v \big|_{lv} = p_{atm}\left(T_{lv}\right) / RT_{lv}$

The mass transport across the interface is modeled by adding mass sources or sinks to the mesh cells adjacent to either side of the interface, following the approach explained in Refs. [43] and [44]:

$$S_{m,g} = \frac{m'' A_{cell}}{V_{cell,g}} \tag{19}$$

$$S_{m,l} = -\frac{m'' A_{cell}}{V_{cell,l}} \tag{20}$$

where A_{cell} is the interface area of the specified cell adjacent to the interface and V_{cell} is the cell volume. Energy transport induced by evaporation and condensation processes are modeled by adding energy sources in the mesh cells adjacent to either side of the interface:

$$S_{h,g} = S_{m,g} h_s \left(T \right) \tag{21}$$

$$S_{h,l} = S_{m,l} h_s \left(T \right) + S_{m,l} h_{f,g} \tag{22}$$

$$h_s \left(T \right) = c_p \left(T - T_{ref,sim} \right) \tag{23}$$

The first term on the right-hand side of equations (21) and (22) represents the sensible heat contributed by the mass source, while the additional term in equation (22)accounts for the latent heat adsorbed/released during evaporation/condensation, where $h_{f,g}$ is the latent heat of

evaporation ($h_{f,g}$ = 2.497 x10^6 J/kg). The temperature T_{ref} in the equation (23) is an arbitrary reference temperature implemented in the simulation, set equal to 0 °C .

3.4. Other boundary conditions

The upper boundary of the gas domain is 15 times larger than the droplet radius and the concentration of vapor at this boundary is calculated as:

$$C_v = \frac{RH\, p_{sat}(T_\infty)}{RT_\infty} \tag{24}$$

where RH is the relative humidity of the air (RH = 30 %) and T_∞ is the temperature of the air in the far-field (T_∞ = -1.5 °C). The contact line temperature measured from the infrared (IR) experiments is used as a time-dependent boundary condition at each cell in the contact line of the droplet domain. At each time step, a user-defined function (UDFs) is used to update the temperature of each cell in the computational domain with its corresponding infrared temperatures from the experiments. To simulate the cooling power provided by the thermoelectric cooling system, a heat transfer coefficient at the bottom wall of the domain is used as a boundary condition; this heat transfer coefficient is estimated such that the temperature drop across the droplets matches with the experiments. Temperature is continuous across all interior boundaries in the domain, thereby assuming that any contact thermal resistances are negligible.

3.5. Initial conditions

At the onset of solidification, the fraction of the droplet that had crystalized during recalescence releases latent heat that locally increases the temperature of the ambient around the droplet. If it were assumed that this process occurs adiabatically, the fraction of ice formed could be simply computed by balancing the latent heat and sensible heat required to increase the temperature of the subcooled droplet to the freezing point. However, our prior study [28] has shown that it is critical to consider energy losses to the surroundings of the droplet in the estimation of this initial fraction of ice. Therefore, the latent heat released during recalescence is equated to the energy losses to the surroundings and the energy required to increase the temperature of the formed ice and the remaining liquid to 0 °C

$$\frac{\rho_l v x \Delta H}{\Delta t_{rec}} = \frac{\rho_l v x c_{p,s} \Delta T}{\Delta t_{rec}} + \frac{\rho_l v (1-x) c_{p,l} \Delta T}{\Delta t_{rec}} + q_{rec,loss} \tag{25}$$

where $x = 1 - \beta$ is the fraction of ice, v is the volume of the droplet before recalescence, Δt_{rec} is the duration of recalescence, and $q_{rec,loss}$ is the total heat transferred to the ambient air and to the substrate during recalescence. This expression requires knowledge of Δt_{rec} and $q_{rec,loss}$; the former is determined from the infrared (IR) temperature measurements during recalescence and the latter is estimated by numerically solving the rate of heat transfer between the droplet at 0 °C and its surroundings under transient conditions. The total recalescence time and the results of the numerical simulations performed to quantify the heat losses during recalescence are presented in Section 4.1. The initial fraction of ice calculated using equation (25) is used as the initial condition in the transient simulation of solidification. To set the initial fraction of ice in the numerical simulations, the T_{sol} and T_{liq} estimated by using equation (1) are inputted as initial conditions to the solidification/melting model.

3.6. Numerical solution settings

The numerical simulations of the transient heat and mass transfer use the SIMPLE algorithm for pressure-velocity coupling and the first order implicit scheme for time discretization, with a time-step of 0.01 s. The mesh used for the case S (shown in Figure 4) has a total of 1,360,000 tetrahedral cells. Similar mesh and domain sizes were employed for case D. The results of the simulations are checked for mesh and domain size independence. Refinement to a mesh with twice as many cells resulted in less than 2% change in the freezing time. Simulations with a domain size increasing from 15 to 30 times the droplet radius show that the freezing time changed within 1%.

4.0. Results

The infrared (IR) surface temperature recordings during the sequential solidification of a pair of adjacent droplets are used to investigate the pathways for heat transfer between the droplets. In Section 4.1, these measurements are used to track the evolution of the crystallization process and to determine the fraction of ice formed during recalescence. In Section 4.2, the model is benchmarked against these measurements, such that in Section 4.3, the simulated temperature, vapor mass fraction, and velocity fields can be used to qualitatively asses the different transport mechanisms at play. Lastly, a quantitative description of each heat transport pathway between a solidifying droplet and its neighbor is provided in Section 4.4.

4.1. *Droplet-to-droplet interactions during recalescence*

A sequence of side-view temperature maps on the surfaces of droplets S1 and S2 are shown in Figure 5 during the recalescence of droplet S1. Prior recalescence at t = 0 s, both droplets are supercooled liquid with an average surface temperature of ~-8.5 °C and have a slight temperature drop (~ 0.5 °C) across the droplet height due to conduction to the substrate. At the onset of the recalescence, at observed at t ~ 0.01 s, ice crystals heterogeneously nucleate near the base of droplet S1 and begin to propagate upward. By t = 0.02 s, a front of ice crystals can clearly be identified as the boundary between the two well-defined temperature regions with uniform temperature; in front of the crystallization front the temperature of the droplet remains at ~-8.5 °C , whereas the temperature within the regions where crystallization has already occurred is close to the equilibrium freezing temperature of 0.0 °C . Subsequently, at t = 0.03 s, the crystallization front has propagated throughout the entire surface of droplet S1, marking the completion of recalescence. The dynamics of the crystallization process observed in the sequence of images in Figure 5 agrees with the decelerating propagation of the crystallization front previously reported in the literature [28,45]; the crystallization front advances faster at the beginning of the recalescence process and then reduces as it progresses toward the top of the droplet.

After droplet S1 has completed recalescence, latent heat released due to crystallization (the portion that is not invested into increasing the sensible temperature of droplet S1) locally heats the environment causing a slight increase of ~0.2 °C in the average surface temperature of droplet S2. Similar crystal growth dynamics and increasing in the temperature of the neighboring droplet are observed in the sequences of side-view surface temperatures during the recalescence of droplets S2, D1, and D2 that are provided in the supplementary information. Although it is often assumed that there is not enough time for heat to dissipate to the environment during the rapid crystallization process, and therefore recalescence occurs adiabatically, comparing to the timescale for heat diffusion from the droplet to its surroundings reveals that some of the heat released should dissipate to the environment. For the experiments considered in this paper, some heat can still diffuse to the substrate even though the maximum recalescence time observed (~ 0.06 s for droplet D1) is slightly smaller than the timescale for heat diffusion in the substrate given by $\tau_\alpha = l^2/\alpha_s \approx 0.12$ s , where α_s = 8.93 × 10^{-5} m^2/s is the thermal diffusivity of the silicon substrate and $l = 2R_{D1}$ = 3.15 × 10^{-3} m is the length scale for heat diffusion in the substrate, and R_{D1} is the radius of droplet D1.

Therefore, recalescence cannot be assumed to occur adiabatically and a fraction of the latent heat released to the substrate should manifest as an increase in the temperature of the neighboring droplet.

The numerical model described in Section 3.5 is used to estimate the heat transferred from a droplet with uniform temperature equal to 0 °C to its environment. The total heat lost to the substrate through the base of the droplet and to the ambient air through the droplet-gas interface is summarized for all of the droplet recalescence events in Table 2, along with their respective time to complete recalescence and fraction of ice crystalized calculated from equation (25). The results indicate that ~75% of the heat released during recalescence is lost to the ambient (substrate and air), whereas only 25% sensibly heats the droplet up to 0 °C. Because recalescence occurs much faster than the time-scale for heat diffusion to the neighboring, only ~0.1% of the heat released by the droplet undergoing recalescence increases the temperature of the neighboring droplet. The amount of heat lost to the ambient, the fraction of ice formed, and the duration of the recalescence process all increase with the size of the droplet; the smallest droplet D2 released 10 times less heat than droplet D1.

4.2. *Droplet surface temperature distributions during solidification*

The measured temperature maps on the surfaces of a solidifying droplet and its neighbor are used to benchmark the numerical simulations. A sequence of side-view surface temperature maps during the sequential solidification of droplets S1 and S2 with similar volume are shown in Figure 6. In the experimental results shown on the left, a vertical line is drawn passing through the centerline of the droplets (based on their shape prior to recalescence) as a reference from which any asymmetry in the final shape of the droplet can be detected. Overall, the numerical predictions shown on the right qualitatively capture all key characteristics of the experimental temperature distributions, with a few differences discussed in detail below.

At the onset of the solidification of droplet S1 (just after recalescence), droplet S2 is in a supercooled liquid state at an average temperature slightly above that of the substrate, while the temperature of droplet S1 is uniform and close to 0 °C. At intermediate times between recalescence and complete solidification, as at t = 3.03 s in Figure 6, the temperature distribution in the solidifying droplet has two well-defined regions separated by the solidification front. A region above the solidification front remains near T_{eq} and a solid region behind the solidification front

has temperature isotherms that decreases in the direction towards the substrate. As this solidification front progresses, the water-ice mixture above the front is pushed upward, increasing the height of the droplet and leading to a frozen droplet with a conically-shaped apex (which is not present in the simulation results because volume changes during solidification are neglected). Although, the numerical simulations reproduce the temperature distributions observed in the experiments, as well as the asymmetric solidification evidenced by the inclination angle of the solidification front with respect to the substrate horizontal, the location of solidification front obtained in the numerical simulations lags behind the experimental results at any given time. This results in slightly longer prediction solidification time of t = 6.22 s in the numerical simulations compared to t = 6.03 s during the experiment. The relative error in the freezing time estimated for all the cases considered in the numerical simulations was below 5%.

In contrast to the symmetrical solidification of individual droplets [28], the presence of a neighboring droplet results in an asymmetric progression of the solidification front with respect to the centerline of the droplet. Close inspection of the temperature contours in Figure 6 reveals that the temperature gradient is steeper in the solid region on the side of the solidifying droplet nearer to its neighbor. The freezing front advances more quickly on this side of the droplet as the latent heat released at the solidification front can be dissipated at a higher rate, which results in the asymmetric progression of the front. At time t = 3.03 s, the dashed line indicates that the solidification front is tilted 0.64 degrees from a horizontal line parallel to the substrate. This asymmetric propagation of the freezing front shifts the conical tip of the frozen droplet in a direction away from its neighbor. This shift is very smaller in the solidification of droplet S1, only 0.05 mm to the left of its initial centerline, whereas the asymmetrical progression of the freezing front is slightly more prominent during the solidification of droplet S2. At time t = 3.03 s, the solidification front within droplet S2 is tilted 1.48 degrees from horizontal, leading to a 0.09 mm shift in its tip to the right. It is worth noting that despite the tips of droplets S1 and S2 moving away from the centerline of the droplet, the internal angle formed by the droplets S1 and S2 tips (approximately 130 degrees for droplet S1 and 135 degrees for droplet S2) upholds the tip angle universality previously reported for symmetrical solidification [31] of a droplet on a horizontal substrate (~139 ± 8 degrees) and asymmetrical solidification [46] of a droplet resting on a tilted substrate (~130 8 degrees)."

The thermography data for the solidification of the differing sized droplets D1 and D2, shown in Figure 7, provide clearer evidence of the asymmetrical freezing that occurs in the presence of a neighboring droplet. The interactions between differing sized droplets leads to more asymmetric freezing behavior compared to the similarly sized droplets. From the sequence of temperature maps shown during the solidification of droplet D1 in Figure 7, it can be observed that the freezing front progresses more rapidly on the side closer to the neighboring droplet D2, which results in asymmetrical solidification of droplet D1 with the solidification front progressing at an tilt angle of 1.79 degrees from horizontal and a final shape with the top shifted 0.14 mm from the centerline. Subsequent solidification of droplet D2 also occurs asymmetrically, with an even more pronounced tilt angle of 2.63 degrees and a tip shift of 0.18 mm away from the centerline. In comparison with case S (droplets with similar size), the asymmetry in the freezing front propagation is more severe for case D. This suggests that the relative size of droplet pairs can have a strong effect on the interactions between the solidifying droplet and its neighbor.

4.3. *Droplet-to-droplet interaction mechanisms*

This section considers the simulated temperature and liquid fraction distributions within the droplets during their sequential solidification, along with the water vapor mass fraction and the velocity vector field in the surrounding gas domain, to identify the heat and mass transport mechanisms that cause asymmetrical. Case D is presented in detail because the interactions are more apparent. Figure 8 shows the time-sequence of simulated contour plots during the solidification of the larger droplet (droplet D1), whereas Figure 9 shows the same set of contour plots during solidification of the smaller droplet (droplet D2). For both droplets, the temperature contours suggest two primary paths for heat exchange between the droplets; (1) heat conduction through the substrate and (2) heat transfer through the air domain. For each these two pathways, there are several mechanisms driving heat exchange between the droplets. Heat conduction in the substrate occurs due to the high local temperature at the base of the solidifying droplet, from which heat can either flow directly through the bottom of the substrate or to the base area of the neighboring droplet at a lower temperature. Heat transfer between the droplets through the air domain occurs due to the temperature and concentration differences between interfaces of the droplets and the far field boundary, which drive coupled heat diffusion, natural convection, and evaporative cooling at the interfaces of the droplets. The influence of each of these transport

mechanisms on the on the thermal coupling between the neighboring droplets during solidification is assessed in the following sections.

4.3.1. Heat diffusion

After recalescence of droplet D1 at t = 0.06 s in Figure 8 (a), the latent heat released increases the temperature of the substrate and the air near the droplet. The temperature difference between the droplet and the lower wall of the substrate drives heat away to the cooling system and spreads the heat laterally. Although the temperature gradient formed within the substrate reaches the region of the substrate below the neighboring droplet, the temperature rise within the neighboring droplet D2 is barely appreciable from the contour plots. At t = 8.06 s, the horizontal temperature isotherms within droplet D1 indicate that the latent heat released at the solidification front is conducted through the part of the droplet that has solidified to the substrate; there is also a significant increase in the temperature of the air around the droplet. Some of this heat is transferred to the neighboring droplet through the air and substrate domains, which leads to a slight increase in the temperature (~1.5 °C) of droplet D2 on its side closer to droplet D1. The liquid-ice mixture region of the droplet ahead of the solidification front that remains near T_{eq} is primarily responsible for increasing the temperature of the air above the droplet by diffusion. As the freezing front advances towards the top of droplet D1, the thermal resistance of the solid part of the droplet increases, reducing the temperature at its base and consequently the heat transfer from droplet D1 to the substrate. After complete solidification, the only a small temperature gradient remains in the droplet due to the temperature difference between the far field and lower wall of the substrate.

During droplet D2 solidification, the sequence of temperature contour plots in Figure 9 (a) show the same mechanisms for heat diffusion observed during the solidification of droplet D1. In this case, the latent heat released by droplet D2 increases the temperature of droplet D1 at t = 1.52 s by ~ 0.7 °C in the regions that are closer to D2.

4.3.2. Heat transport in the gas domain

Natural convection in the air domain is driven by the temperature difference between the droplet-gas interface of the solidifying droplet and its surroundings. Differences in air density caused by the temperature field induce flow above the freezing droplet, with characteristics that depend on the stage of the solidification process. At t =0.06 s, just after recalescence, the velocity vector field shown in Figure 8 (b) corresponds to the airflow expected for natural convection above

a *finite* cooled substrate (air flowing downwards from far field toward the substrate to replace cold air that moves laterally), with an average velocity of 0.3 mm/s in the region above the droplet. At later times between recalescence and complete solidification (e.g., t = 8.06 s in Figure 8 (b)), a density gradient created by heating of the air above the droplet D1 drives and upward flow with an average velocity of about 3.0 mm/s that draws in cooler air flow from the sides of the droplet . This natural convection current provides additional cooling at the interface of droplet D1, which results in additional phase change in the liquid-ice mixture region at the top of droplet above the solidification front (as can be observed from the liquid fraction contours plotted within the droplet in Figure 8 (b)). On the surface of droplet D2, natural convection cooling competes with heat diffusing from droplet D1. After droplet D1 has solidified at t = 15.06 s, the air flows from the far field towards the substrate at an average velocity of 0.6 mm/s.

Relative to the natural convection-induced cooling caused by the solidification of droplet D1, the solidification of droplet D2 has a smaller effect on the surrounding velocity field. The velocity vectors are shown in Figure 9 (b) during the solidification of droplet D2. At the start and the end of the solidification process, the velocity fields resemble typical natural convection profile over a finite cooled substrate, just as during the solidification of droplet D1. At an intermediate step during the solidification of droplet D2, such as at t = 1.52 s, heating of the air above the droplet induces a small recirculation zone, but only on the right side of droplet D2; the additional cooling by this convection causes additional solidification in the top of the droplet.

4.3.3. Mass transport in the gas domain and evaporative cooling at the gas-droplet interface

A time-sequence of mass vapor fraction contour plots in the gas domain is shown in Figure 8 (c) for the solidification of droplet D1. The difference between the water vapor concentration in the ambient and droplet-gas interfaces of the droplets drives vapor transport via combined diffusion and natural convection. At the onset of the solidification process, the concentration of water vapor on the surface of the droplet D1 is uniform and equal to 3.7×10^{-3}. This relatively high concentration of water vapor in the vicinity of droplet D1 also increases the concentration of vapor around droplet D2. The gradients of vapor mass fraction indicate that most of the surface area of the droplets lose vapor to the ambient, but a small section of droplet D1 loses vapor to droplet D2 through the region between the droplets. After the solidification process is complete, the interfaces of both droplets are cooled down to a temperature close to the temperature of the substrate. A small evaporative flux from droplet D2 to droplet D1 is caused by the difference in

the saturation pressure above ice (droplet D1) being smaller than the saturation pressure above a liquid surface (droplet D2) at the same temperature.

During the solidification of droplet D2 (Figure 9 (b)), droplet D1 enhances evaporation on regions of the surface of droplet D2 that are closer to droplet D2e Throughout droplet D2 solidification, in the region above the solidification front that is facing droplet D2, the concentration of water vapor decreases from 3.7×10^{-3} to the mass fraction of water above droplet D1, 1.8×10^{-3}. Whereas in regions around droplet D2 that are away from droplet D1, the water vapor concentration reduces gradually to the far-field water vapor concentration. The additional cooling created by this non-uniform evaporation, contributes to additional solidification on the regions of droplet D2 that are closer to D1, as can be observed from the liquid fraction contours at $t = 1.52$ s shown in Figure 9 (b). These differences in the behavior of droplet D1 and D2 reveal how the relative droplet size can affect the contribution of evaporative cooling to the asymmetrical solidification observed during the experiments. Namely, even though droplet D1 solidification is accompanied by stronger evaporative cooling than droplet D2 solidification, the non-uniform solidification induced by evaporative cooling is stronger for droplet D2.

4.4. Quantifying the interactions between a freezing droplet and its neighbor

The results of the numerical simulations are used to quantitatively determine the fraction of latent heat released during droplet freezing that is transferred to its neighboring droplet, as well as the relative strength of the mechanisms that contribute to the asymmetrical solidification in adjacent droplets. Figure 10 plots the total heat transfer rates integrated across the base contact area with the substrate and separately across the droplet-gas interfaces of droplets D1 and D2 at each time-step during the solidification of droplet D1(case D). The total heat transfer rate across the droplet-gas interfaces of each droplet includes combined heat diffusion and natural convection, as well as evaporation cooling. As shown in Figure 10 (a), at the onset of the solidification of droplet D1, the rate at which latent heat is transferred to the substrate and gas is maximum and decreases as the solidification front progresses. As it was discussed in Sections 4.3, heat diffusion to the solid substrate during the solidification of droplet D1 is limited by the thermal resistance of the solid part of the droplet behind the solidification front, which increases as the solidification front progresses towards the top of the droplet. Meanwhile, heat transfer across the droplet interface reduces (not visible in Figure 10 due to the scale of vertical axis) due to the combined effects of: (1) heat and mass diffusion becoming confined to the upper section of the droplet surface

ahead of the solidification front where the temperature is higher and (2) a reduction of the convective heat and mass transport that results from the decreases in the velocity of the dry air drawn in from the sides of the droplet. Throughout the solidification process of droplet D1, the heat transfer lost to the substrate is at least an order of magnitude greater than the heat transfer through the interface of the droplet. A very small fraction of ~0.02% of the heat lost from droplet D1 is ultimately transferred to droplet D2. As shown in Figure 10 (b), the maximum rate of heat transfer to droplet D2 through the substrate (~0.5 mW) occurs at the onset of droplet D1 solidification and decreases the solidification process in droplet D1 progresses. At t = 2 s, the latent heat transferred from droplet D1 is smaller than the heat lost from the base of droplet D2 to the cooling system, leading to a negative heat transfer rate (i.e., net outflow from droplet D2) and decreasing the temperature at the base of droplet D2. Similarly, the interface of D2 is heated at the onset of solidification with about 0.1 mW of power, and rapidly decreases as the solidification front of droplet D2 advances.

The same integrated heat transfer rates through the droplet bases and interfaces during the solidification of droplet D2 are shown in Figure 11. Generally, all of the trends and mechanisms are similar to those shown in Figure 10, so they are not repeated here. Because droplet D2 is ~11 times smaller than droplet D1, the latent heat of solidification released by droplet D2 is much smaller than droplet D1. Consequently, the rate of heat transfer at the base of droplet D2 is 5 times smaller than during the solidification of D1 shown in Figure 10 (a). However, the fraction of heat lost from droplet D2 to the neighboring droplet D1 is larger; approximately 6.6% of the latent heat released by droplet D2 is transferred to droplet D1. This demonstrates that a larger droplet has a greater impact on the solidification of smaller neighboring droplet and vice versa.

The heat transfer rates presented in Figure 10 and Figure 11 allow determination of the amounts of heat transferred to the neighboring droplet through each pathway. For solidification of droplets D1 and D2, the Sankey diagram in Figure 12 summarize the percentages of the total latent heat released during recalescence through each of the heat transfer pathways to the neighboring droplet. During the recalescence of both droplets D1 and D2, ~9% of the latent available is invested into sensible heating of the droplets up to T_{eq}. Meanwhile, ~20-30 % of the heat is lost to the substrate and a very small fraction to the ambient air. During the solidification process of droplet D1, a total of 2.6% of the latent heat available is lost to the ambient air (1.4% via combined heat diffusion and natural convection, and 1.2 % via evaporative cooling); the remaining 68.6% of the heat

conducts away through the substrate. Ultimately, only 0.7% of the total latent heat is transferred to the neighboring droplet, with most of that heat being transferred through the substrate (0.5%) versus through the air (0.2%). In comparison with droplet D1, during the freezing of droplet D2, a larger percentage of the heat is transfer to its neighbor. A total 6.6% of the latent heat released by droplet D2 is transferred to droplet D1, with close to a 1:1 split between the amount transferred through the substrate and air domains. As it was shown in Section 4.3, asymmetric heat exchange through the substrate and ambient air leads to non-uniform rates of solidification within a freezing droplet, with smaller droplets freezing in the neighborhood of a larger droplet having a more drastic asymmetry. Here, the quantitative delineation between the heat transport pathways confirms how smaller droplets have stronger interactions with their large neighbors.

5.0. Conclusions

This paper illustrates the pathways of heat and mass exchange between a freezing droplet and an adjacent neighboring droplet, which lead to asymmetrical solidification. Infrared (IR) thermography measurements of the surface temperature of the freezing droplet and its neighbor, along with high-fidelity numerical simulations, are used to calculate the amount of heat transferred to the neighboring droplet through the substrate and ambient air. The modeling approach presented in this paper uses the IR temperature data at the contact line of the droplet as a boundary condition and provides a full description of the driving mechanisms for heat and mass exchange between the freezing droplet, substrate, ambient air, and neighboring droplet. The results of the numerical simulations are benchmarked against the experiments, showing good agreement in the evolution of the surface temperature maps of the droplets.

The infrared temperature maps on the surfaces of the droplets indicate that non-uniform heat transfer at the solidification front of a freezing droplet leads to an asymmetrical solidification with the conical tip of the final frozen droplet shape shifted away from its neighbor. The impact of droplet size on the relative severity of the asymmetry was evaluated by solidifying pairs of droplets that were similar in size (~1:1 ratio) and dissimilar in size (~10:1 ratio). The results show that asymmetries in the solidification process intensify when the size of one droplet is small relative to its neighbor.

The heat transfer rates through the base and interface of the droplets were numerically integrated from the simulations to quantify the amount of heat exchange between the droplets. The

simulation results indicate that less than 1% of the latent heat released by a large droplet is transferred to a smaller neighbor, whereas the smaller neighbor will transfer ~6% of the latent heat released to the larger droplet. The transient evolution of temperature and liquid fraction within the droplets obtained from the numerical simulations, as well as the vapor mass fraction and velocity fields in the ambient air, reveal that the presence of a neighboring droplet causes non-uniform cooling at the droplet-gas interface and non-uniform heat spreading into the substrate, which are the mechanisms responsible for the asymmetrical solidification.

The experimental and modeling approaches presented in this manuscript lay the groundwork for future investigations of additional parameters that influence the interactions between the droplets such as the droplet pitches, substrate thermal conductivity, and substrate wettability. Furthermore, the results presented in this paper offer mechanistic insights that may assist in engineering surfaces that delay the propagation of frost by controlling the intensity of the interactions of between the droplets.

Acknowledgments

The first author acknowledges financial support provided by the Colombian Department for Science, Technology and Innovation (Colciencias), Fulbright-Colombia, and the Colombia-Purdue Institute (CPI).

References

[1] Y. Cao, Z. Wu, Y. Su, Z. Xu, Aircraft flight characteristics in icing conditions, Progress in Aerospace Sciences. 74 (2015) 62–80.
[2] O. Parent, A. Ilinca, Anti-icing and de-icing techniques for wind turbines: Critical review, Cold Regions Science and Technology. 65 (2011) 88–96.
[3] S. Jhee, K.-S. Lee, W.-S. Kim, Effect of surface treatments on the frosting/defrosting behavior of a fin-tube heat exchanger, International Journal of Refrigeration. 25 (2002) 1047–1053.
[4] K. Nawaz, A.F. Elatar, B.A. Fricke, A critical literature review of defrost technologies for heat pumps and refrigeration systems, Oak Ridge National Lab. (ORNL), Oak Ridge, TN (United States), 2018.
[5] J.L. Laforte, M.A. Allaire, J. Laflamme, State-of-the-art on power line de-icing, Atmospheric Research. 46 (1998) 143–158.
[6] J. Andrey, O. Richard, Relationship between weather and road safety: past and future research directions, Climatological Bulletin. 24 (1990) 66.

[7] Frankenstein Susan, Tuthill Andrew M., Ice adhesion to locks and dams: past work; future directions?, Journal of Cold Regions Engineering. 16 (2002) 83–96.
[8] C.C. Ryerson, Ice protection of offshore platforms, Cold Regions Science and Technology. 65 (2011) 97–110.
[9] M. Amer, C.-C. Wang, Review of defrosting methods, Renewable and Sustainable Energy Reviews. 73 (2017) 53–74.
[10] K.W.F. Howard, P.J. Beck, Hydrogeochemical implications of groundwater contamination by road de-icing chemicals, Journal of Contaminant Hydrology. 12 (1993) 245–268.
[11] I.A. Munck, C.M. Bennett, K.S. Camilli, R.S. Nowak, Long-term impact of de-icing salts on tree health in the Lake Tahoe Basin: Environmental influences and interactions with insects and diseases, Forest Ecology and Management. 260 (2010) 1218–1229.
[12] L. Fay, X. Shi, Environmental impacts of chemicals for snow and ice control: State of the knowledge, Water Air Soil Pollution. 223 (2012) 2751–2770.
[13] J.L. Hoke, J.G. Georgiadis, A.M. Jacobi, Effect of Substrate Wettability on Frost Properties, Journal of Thermophysics and Heat Transfer. 18 (2004) 228–235.
[14] B. Na, R.L. Webb, A fundamental understanding of factors affecting frost nucleation, International Journal of Heat and Mass Transfer. 46 (2003) 3797–3808.
[15] Q. Zhang, M. He, X. Zeng, K. Li, D. Cui, J. Chen, J. Wang, Y. Song, L. Jiang, Condensation mode determines the freezing of condensed water on solid surfaces, Soft Matter. 8 (2012) 8285–8288.
[16] P. Tourkine, M. Le Merrer, D. Quéré, Delayed freezing on water repellent materials, Langmuir. 25 (2009) 7214–7216.
[17] J.B. Boreyko, C.P. Collier, Delayed frost growth on jumping-drop superhydrophobic surfaces, ACS Nano. 7 (2013) 1618–1627.
[18] X. Chen, R. Ma, H. Zhou, X. Zhou, L. Che, S. Yao, Z. Wang, Activating the microscale edge effect in a hierarchical surface for frosting suppression and defrosting promotion, Scientific Reports. 3, 2515 (2013).
[19] X. Sun, K. Rykaczewski, Suppression of frost nucleation achieved using the nanoengineered integral humidity sink effect, ACS Nano. 11 (2017) 906–917.
[20] J.B. Boreyko, R.R. Hansen, K.R. Murphy, S. Nath, S.T. Retterer, C.P. Collier, Controlling condensation and frost growth with chemical micropatterns, Scientific Reports. 6 (2016)
[21] S. Nath, S.F. Ahmadi, J.B. Boreyko, A review of condensation frosting, Nanoscale and Microscale Thermophysical Engineering. 21 (2017) 81–101.
[22] S. Chavan, D. Park, N. Singla, P. Sokalski, K. Boyina, N. Miljkovic, Effect of latent heat released by freezing droplets during frost wave propagation, Langmuir. (2018).
[23] S. Jung, M.K. Tiwari, N.V. Doan, D. Poulikakos, Mechanism of supercooled droplet freezing on surfaces, Nature Communications. 3 (2012) 615.
[24] G. Chaudhary, R. Li, Freezing of water droplets on solid surfaces: An experimental and numerical study, Experimental Thermal and Fluid Science. 57 (2014) 86–93.
[25] X. Zhang, X. Liu, X. Wu, J. Min, Simulation and experiment on supercooled sessile water droplet freezing with special attention to supercooling and volume expansion effects, International Journal of Heat and Mass Transfer. 127 (2018) 975–985.
[26] S. Jung, M.K. Tiwari, D. Poulikakos, Frost halos from supercooled water droplets, Proceedings of the National Academy of Sciences. 109 (2012) 16073–16078.
[27] W. Kong, H. Liu, A theory on the icing evolution of supercooled water near solid substrate, International Journal of Heat and Mass Transfer. 91 (2015) 1217–1236.

[28] J.E. Castillo, Y. Huang, Z. Pan, J.A. Weibel, Quantifying the pathways of latent heat dissipation during droplet freezing on cooled substrates, International Journal of Heat and Mass Transfer. 164 (2021) 120608.
[29] T.V. Vu, K.V. Dao, B.D. Pham, Numerical simulation of the freezing process of a water drop attached to a cold plate, Journal of Mechanical Science and Technology. 32 (2018) 2119–2126.
[30] J.H. Snoeijer, P. Brunet, Pointy ice-drops: How water freezes into a singular shape, American Journal of Physics. 80 (2012) 764–771.
[31] A.G. Marín, O.R. Enríquez, P. Brunet, P. Colinet, J.H. Snoeijer, Universality of Tip Singularity Formation in Freezing Water Drops, Physics Review Letters. 113 (2014) 054301.
[32] Z. Jin, S. Jin, Z. Yang, Visualization of icing process of a water droplet impinging onto a frozen cold plate under free and forced convection, Journal of Visualization. 16 (2013) 13–17.
[33] T.V. Vu, Fully resolved simulations of drop solidification under forced convection, International Journal of Heat and Mass Transfer. 122 (2018) 252–263.
[34] G. Graeber, T.M. Schutzius, H. Eghlidi, D. Poulikakos, Spontaneous self-dislodging of freezing water droplets and the role of wettability, Proceedings of the National Academy of Sciences. 114 (2017) 11040–11045.
[35] S. Nath, S.F. Ahmadi, J.B. Boreyko, How ice bridges the gap, Soft Matter. 16 (2020) 1156–1161.
[36] G. Graeber, V. Dolder, T.M. Schutzius, D. Poulikakos, Cascade freezing of supercooled water droplet collectives, ACS Nano. 12 (2018) 11274–11281.
[37] ANSYS, Inc., ANSYS FLUENT 19.4 User's Guide, (2019).
[38] V.R. Voller, C. Prakash, A fixed grid numerical modelling methodology for convection-diffusion mushy region phase-change problems, International Journal of Heat and Mass Transfer. 30 (1987) 1709–1719.
[39] V.R. Voller, C.R. Swaminathan, Eral source-based method for solidification phase change, Numerical Heat Transfer, Part B: Fundamentals. 19 (1991) 175–189.
[40] V.R. Voller, M. Cross, N.C. Markatos, An enthalpy method for convection/diffusion phase change, International Journal for Numerical Methods in Engineering. 24 (1987) 271–284.
[41] S. Nath, J.B. Boreyko, On Localized Vapor Pressure Gradients Governing Condensation and Frost Phenomena, Langmuir. 32 (2016) 8350–8365.
[42] D.M. Murphy, T. Koop, Review of the vapour pressures of ice and supercooled water for atmospheric applications, Quarterly Journal of the Royal Meteorological Society. 131 (2005) 1539–1565.
[43] H. Wang, J.Y. Murthy, S.V. Garimella, Transport from a volatile meniscus inside an open microtube, International Journal of Heat and Mass Transfer. 51 (2008) 3007–3017.
[44] Z. Pan, S. Dash, J.A. Weibel, S.V. Garimella, Assessment of water droplet evaporation mechanisms on hydrophobic and superhydrophobic substrates, Langmuir. 29 (2013) 15831–15841.
[45] S. Jung, M. Dorrestijn, D. Raps, A. Das, C.M. Megaridis, D. Poulikakos, are superhydrophobic surfaces best for icephobicity?, Langmuir. 27 (2011) 3059–3066.
[46] M.F. Ismail, P.R. Waghmare, Universality in freezing of an asymmetric drop, Applied Physics Letters. 109 (2016) 234105.

Figures

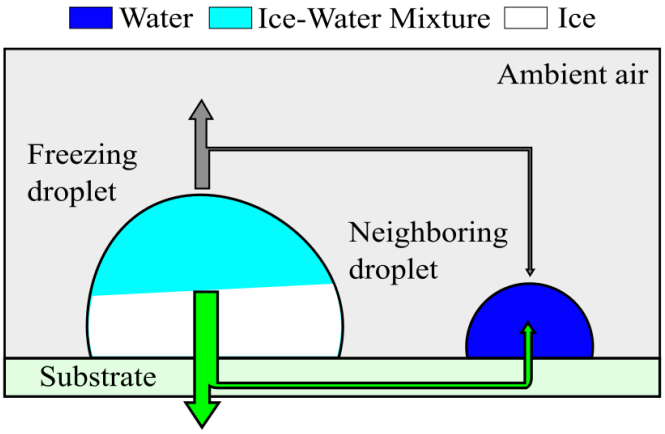

Figure 1. Schematic diagram illustrating two pathways for latent heat dissipation from a freezing droplet to a neighboring liquid droplet, namely heat transfer through the ambient air and heat transfer through the substrate.

Note for the editor: Single column figure

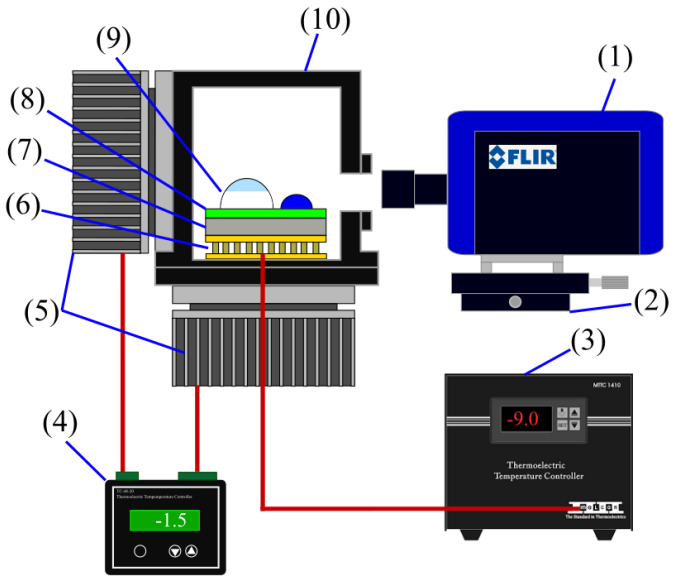

Figure 2. Schematic diagram of the experimental facility used for infrared thermography (IR) measurements during droplet freezing: (1) Infrared camera, (2) translational stages, (3) substrate temperature controller, (4) enclosure temperature controller, (5) thermoelectric stages, (6) thermoelectric plate, (7) sample holder, (8) substrate, (9) droplets, and (10) metal enclosure.

Note for the editor: Single column figure

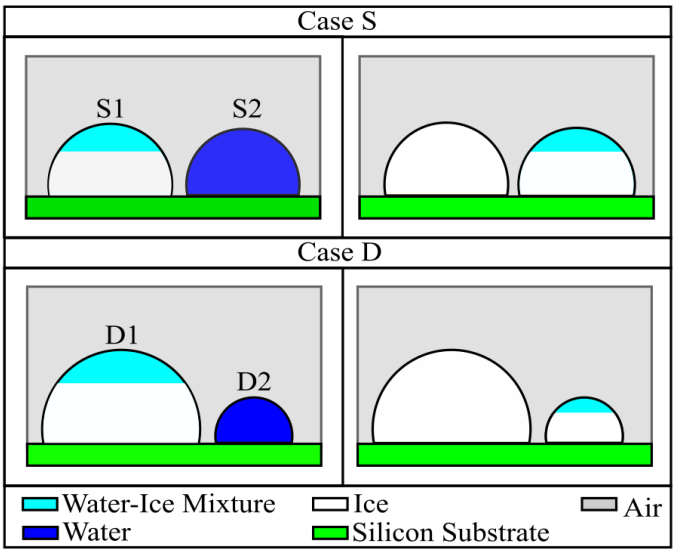

Figure 3. Schematic representation of the two-droplet sequential solidification cases examined in this paper. Case (S) considers a pair of droplets that are similar in size, with volumes 2.88 μL (droplet S1) and 2.52 μL (droplet S2). The panel on the left illustrates the solidification of droplet S1 while droplet S2 remains supercooled liquid, followed by the solidification of droplet S2 illustrated in the right panel. Case (D) considers a larger 8.98 μL droplet (D1) with a smaller 0.76 μL neighboring droplet (D2) that solidify in the same sequence.

Note for the editor: Single column figure

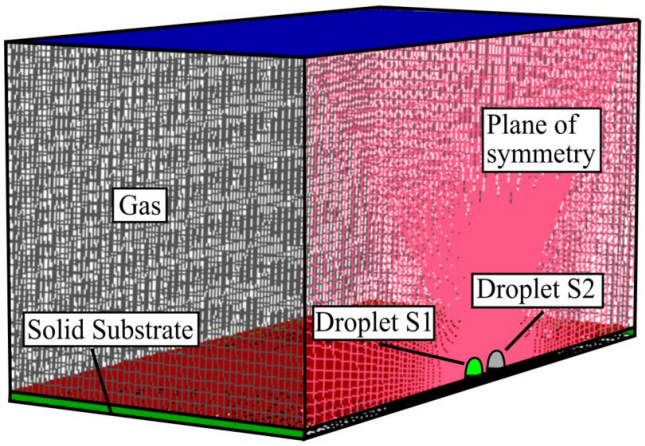

(a)

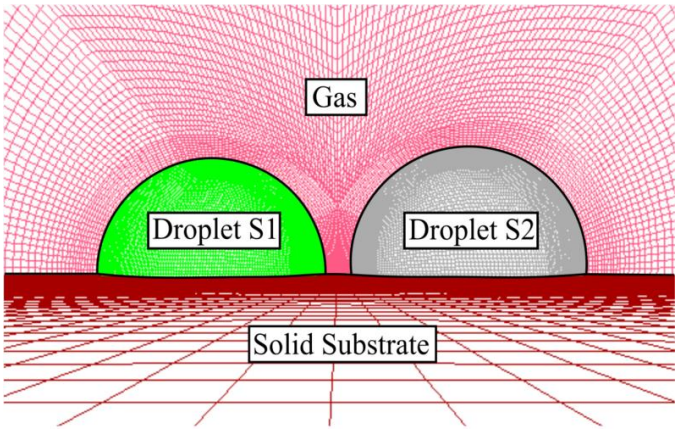

(b)

Figure 4. Numerical solution domain with mesh overlay showing the (a) half symmetric domain along with (b) details near the droplets resting on the surface from a perspective view along the substrate.

Note for the editor: Single column figure

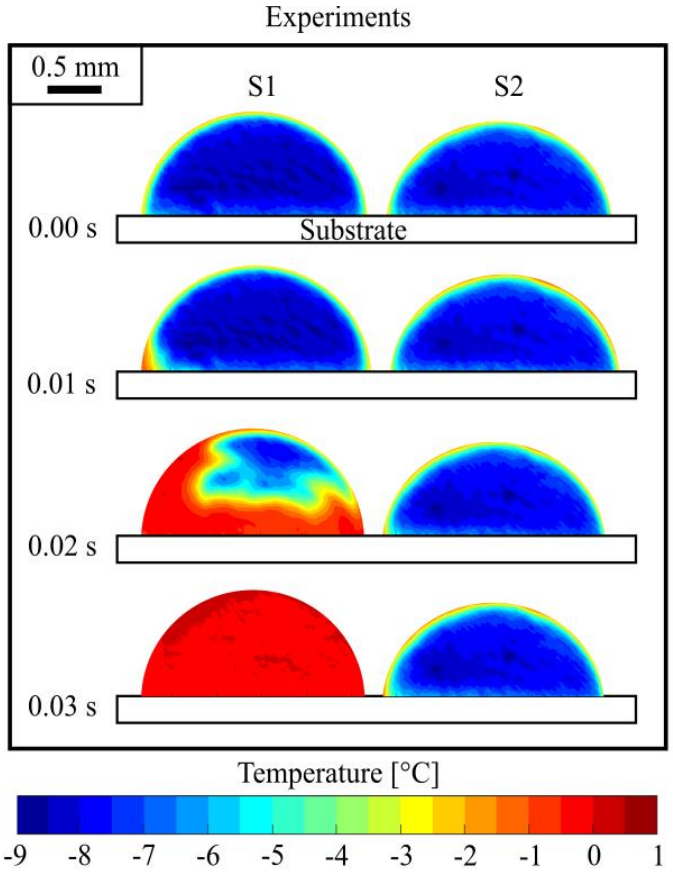

Figure 5. Sequence of experimentally measured side-view infrared temperature distributions on the surfaces of droplet S1 and its neighboring droplet S2. In this sequence of images, droplet S1 is undergoing recalescence while droplet S2 remains in a supercooled liquid state. The silicon substrate size and thickness is not drawn to scale.

Note for the editor: Single column figure

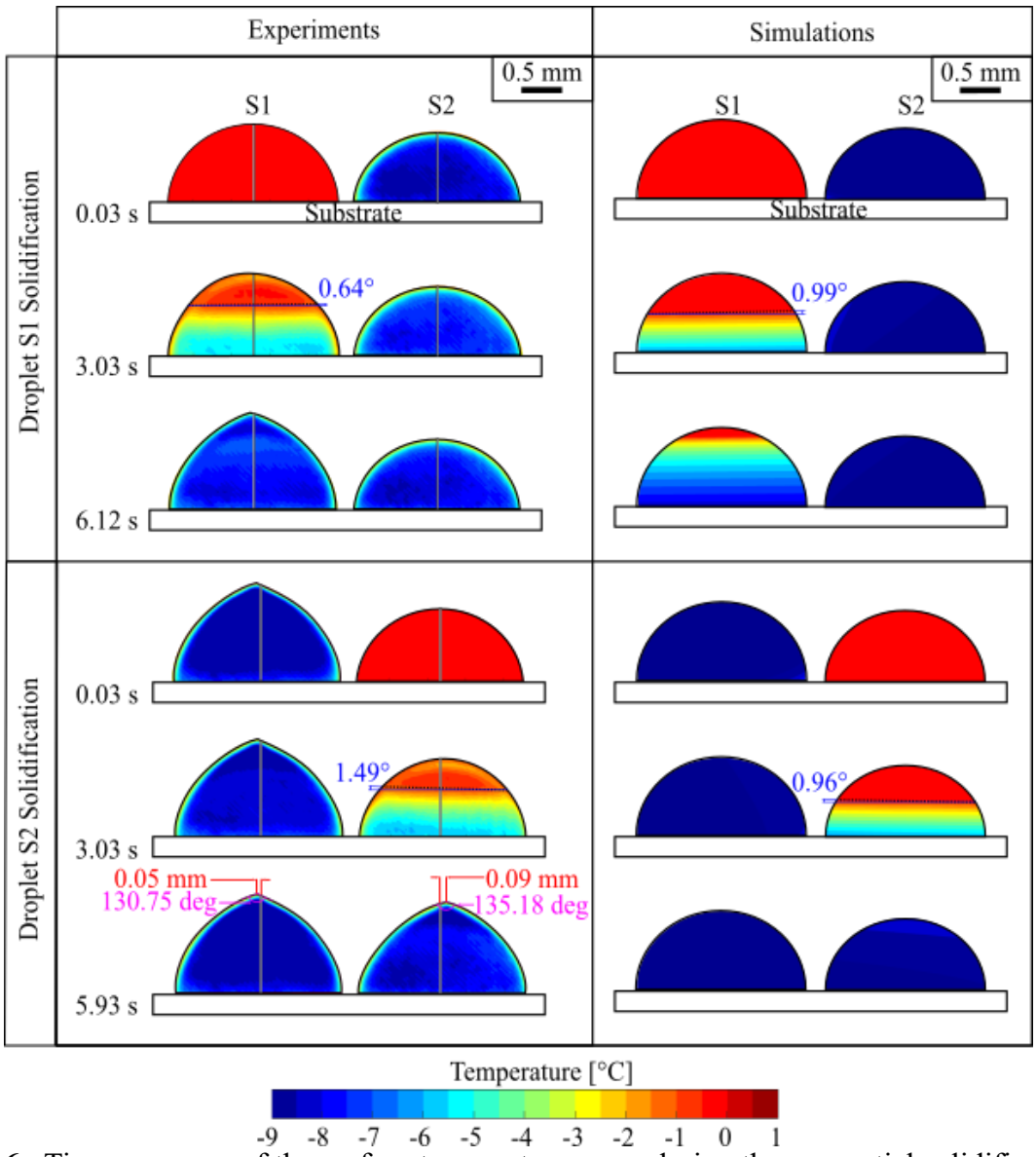

Figure 6. Time sequence of the surface temperature maps during the sequential solidification of similarly sized droplets S1 and S2. The experimental data are shown in the left column and the simulation predictions in the right column. The top row shows the solidification of droplet S1 (where droplet S2 is subcooled liquid) and the bottom row the subsequent solidification of droplet S2 (where droplet S1 is frozen). The experimental IR thermography data is cropped around the droplets to remove the immaterial background data. The vertical lines overlapping the experimental images pass through the centerline of each droplet based on their pre-recalescence shape.

Note for the editor: 1.5 column figure

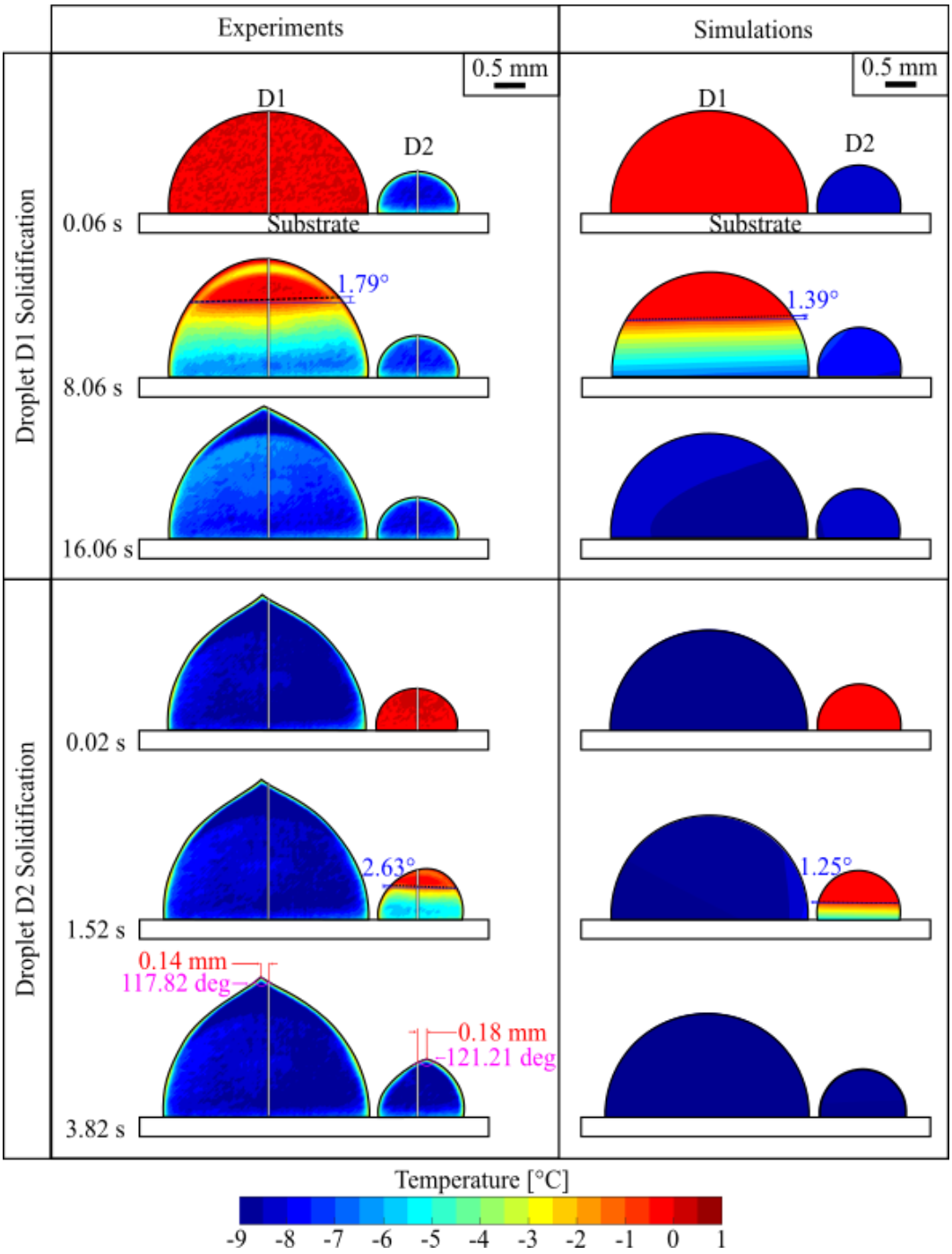

Figure 7. Time sequence of the surface temperature maps during the sequential solidification of differently sized dropletsD1 and D2. The experimental data are shown in the left column and the simulation predictions in the right column. The top row shows the solidification of droplet D1 (where droplet D2 is subcooled liquid) and the bottom row the subsequent solidification of droplet D2 (where droplet D1 is frozen). The experimental IR thermography data is cropped around the droplets to remove the immaterial background data. The vertical lines overlapping the experimental images pass through the centerline of each droplet based on their pre-recalescence shape.

Note for the editor: 1.5 column figure

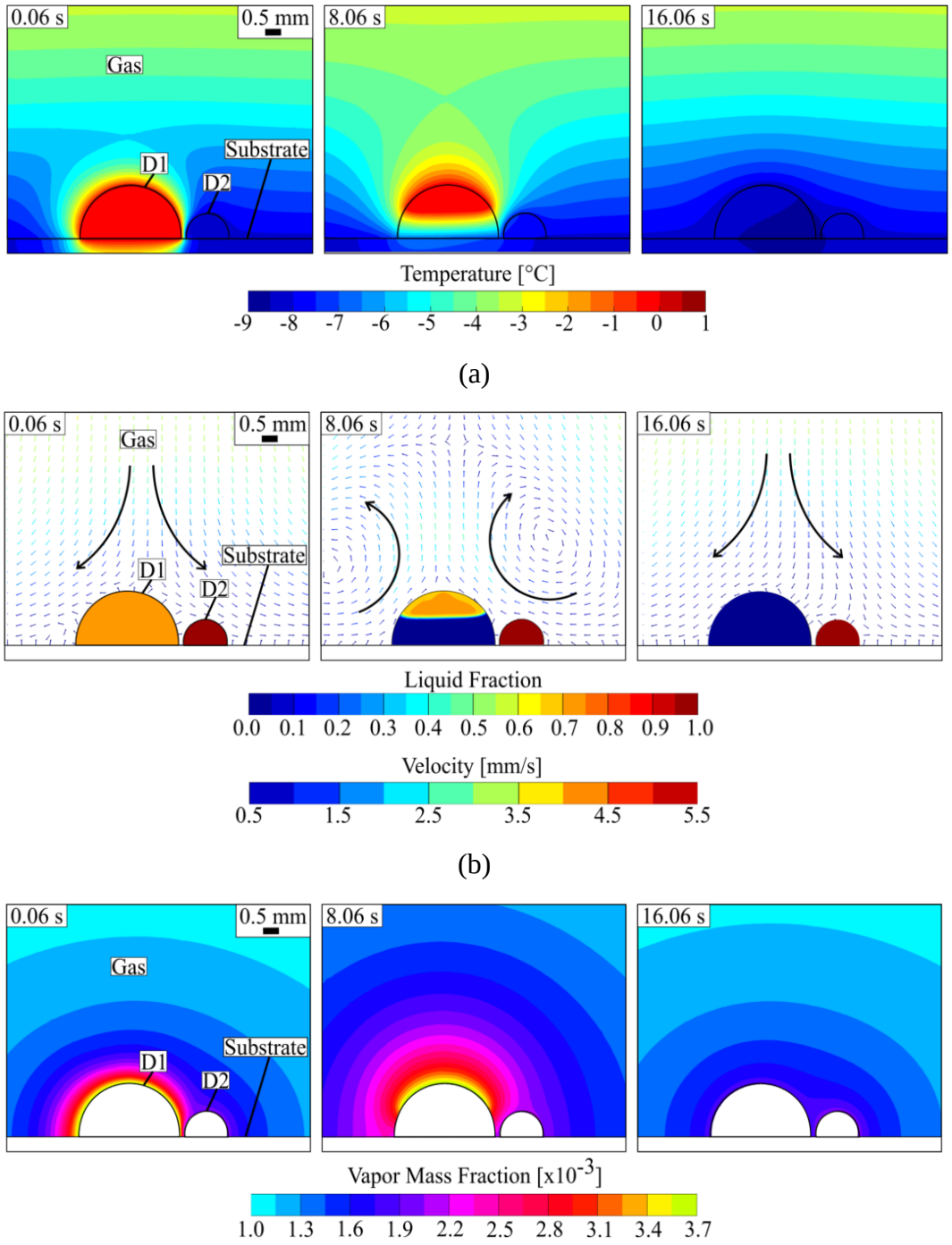

Figure 8. Simulated time sequence of (a) temperature contour plots, (b) liquid fraction contour plots (within the droplets) and velocity vectors (in the gas domain), and (c) vapor mass fraction contour plots (in the gas domain) for the solidification of droplet D1.

Note for the editor: 1.5 column figure

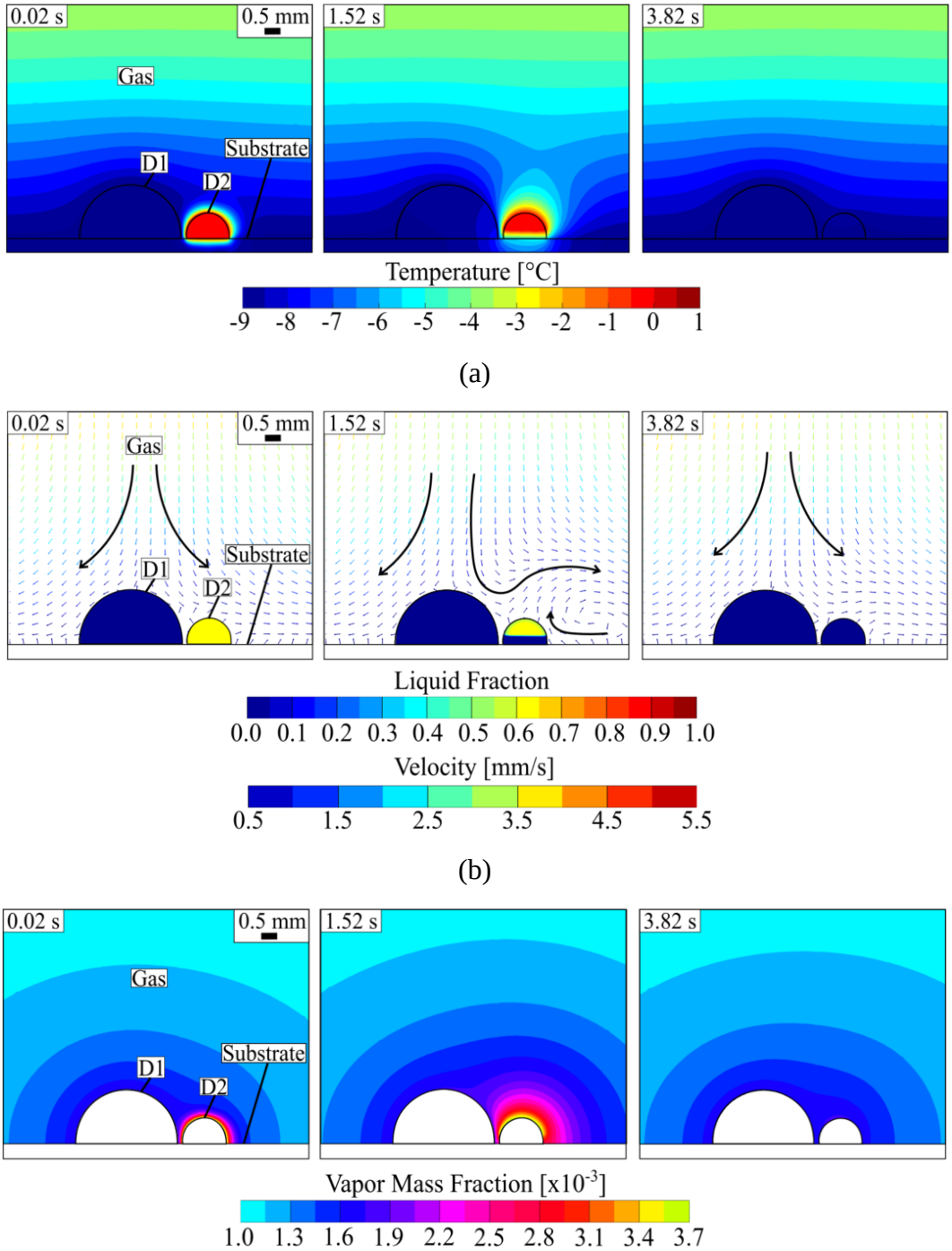

Figure 9. Simulated time sequence of (a) temperature contour plots, (b) liquid fraction contour plots (within the droplets) and velocity vectors (in the gas domain), and (c) vapor mass fraction contour plots (in the gas domain) for the solidification of droplet D2.

Note for the editor: 1.5 column figure

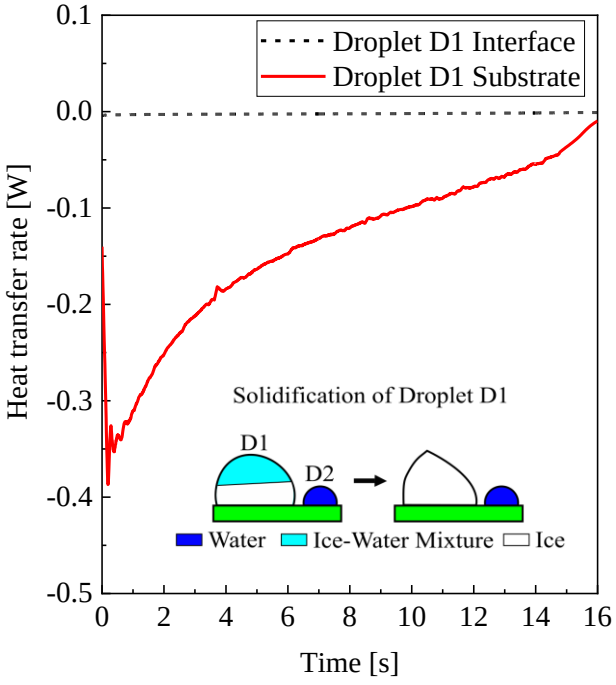

(a)

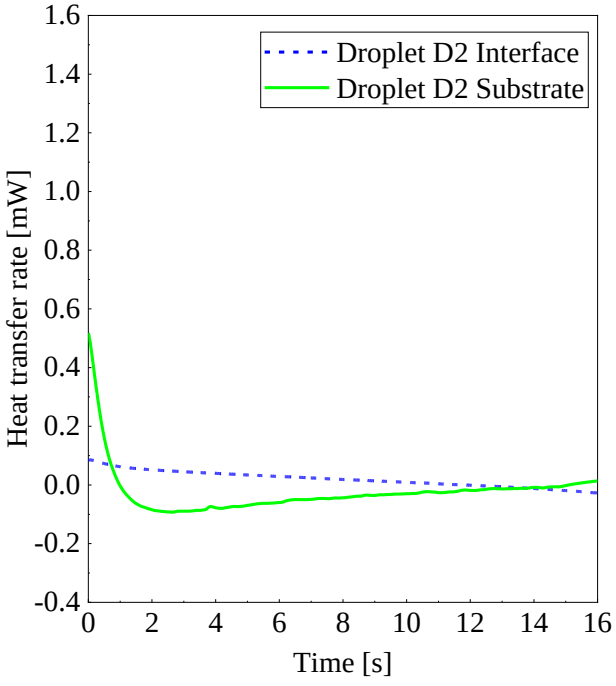

(b)

Figure 10. Heat transfer rate across the droplet base contact area with the substrate (solid lines) and through the droplet-gas interface (dashed lines) of droplets (a) D1 and (b) D2, during the solidification of droplet D1.

Note for the editor: Single column figure

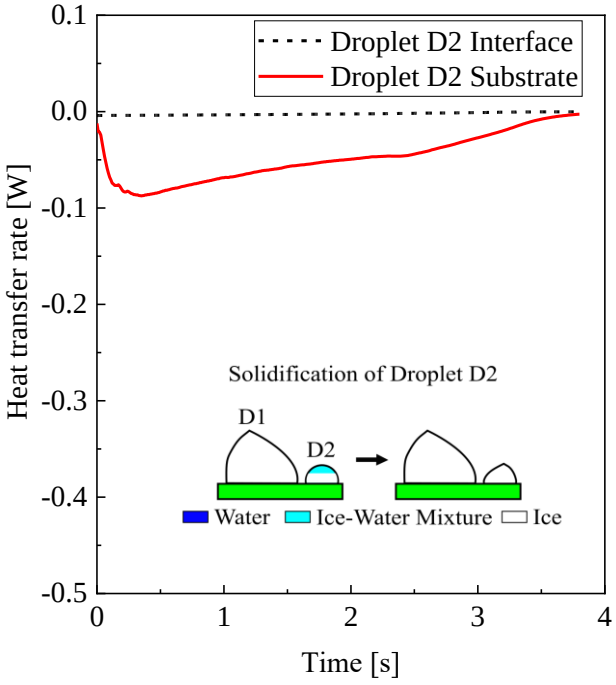

(a)

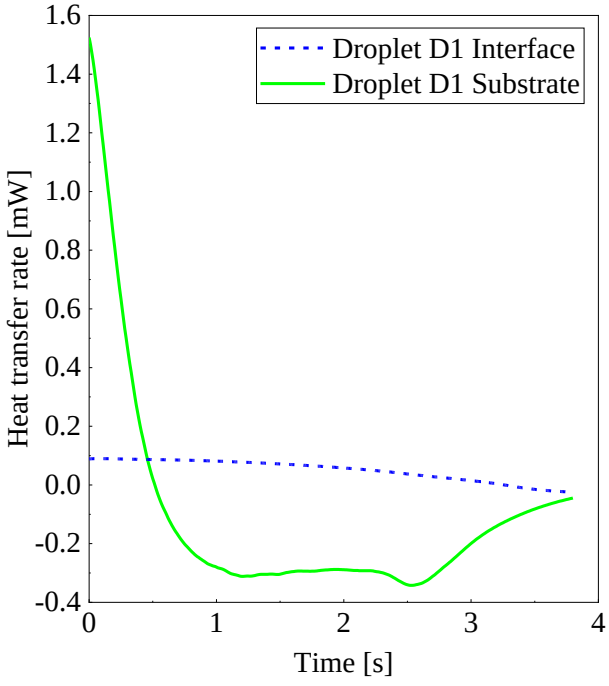

(b)

Figure 11. Heat transfer rate across the droplet contact area with the substrate (solid lines) and through the droplet-gas interface (dashed lines) of droplet (a) D2 and (b) D1, during the solidification of droplet D2.

Note for the editor: Single column figure

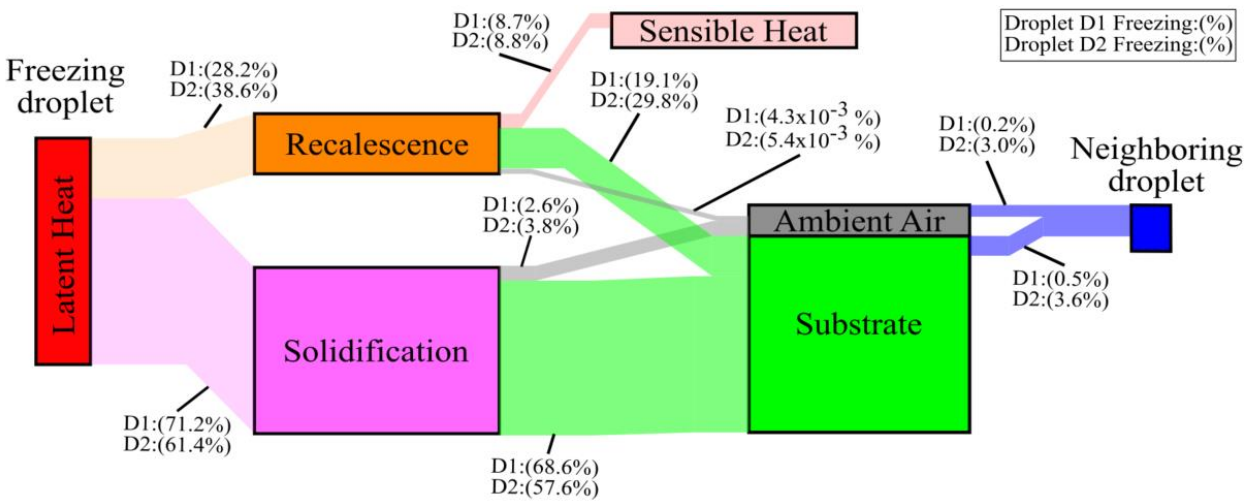

Figure 12. Sankey diagram for the pathways of latent heat dissipation from a freezing droplet to an adjacent neighboring droplet. The percentages of latent heat released are shown for the solidification of a large droplet D1 in the presence of a small supercooled liquid droplet D2 (top labels) and of a small droplet D2 in the presence of a large frozen droplet D1 (bottom labels).

Note for the editor: 2 column figure

Tables

Table 1. Thermophysical properties used in the simulations.

Properties	Water	Ice	Gas	Substrate
density, ρ (kg/m^3)	999.8 at 0.1 °C	917.5 at -5 °C	1.298 at -1.5 °C	2329
thermal conductivity, k (W/m K)	0.58	2.25	0.0242	148
thermal capacity, c_p (J/K kg)	4191	2027	1006	711.6

Table 2. Summary of test results for the interactions between neighboring droplets during recalescence of droplets S1, S2, D1 and D2.

	S1	**S2**	**D1**	**D2**
Droplet volume, v (μL)	2.88	2.52	8.8	0.8
Recalescence time, Δt_{rec} (s)	0.03	0.03	0.06	0.02
Latent heat released during recalescence (J)	0.35	0.3	0.85	0.1
Sensible heat (J)	0.09	0.08	0.27	0.02
Heat loss to the ambient(J)	0.27	0.23	0.61	0.08
Initial fraction of ice, x	0.36	0.35	0.28	0.39
Heat transferred to neighboring droplet ($x10^{-3}$ J)	0.36	0.25	0.46	0.28